The following resources related to this article are available online at
www.sciencemag.org (this information is current as of October 22, 2007):

Updated information and services, including high-resolution figures, can be found in the online
version of this article at:
http://www.sciencemag.org/cgi/content/full/276/5314/926

This article has been **cited by** 3 articles hosted by HighWire Press; see:
http://www.sciencemag.org/cgi/content/full/276/5314/926#otherarticles

This article appears in the following **subject collections**:
Chemistry
http://www.sciencemag.org/cgi/collection/chemistry

Information about obtaining **reprints** of this article or about obtaining **permission to reproduce**
this article in whole or in part can be found at:
http://www.sciencemag.org/about/permissions.dtl

the silica surface, which is approximately equal to four monolayers of water. This suspension was then treated with 20 ml of TMMPS, stirred overnight at room temperature, and heated to reflux for 4 hours. After cooling to room temperature, the mixture was filtered and washed thoroughly with 2-propanol and dried under vacuum to yield 6.2 g of derivatized material.

6. D. G. Kurth and T. Bein, *Langmuir* **9**, 2965 (1993).
7. The population density of organic monolayers for 100% coverage on silica was determined using ¹³C solid-state NMR methods on dense fumed silica spheres with a known surface area (150 m² g⁻¹) and tetrakis(trimethylsilyl)silane [(TMS)₄Si] as an internal standard. Integration of the peaks from functionalized monolayers and from the internal standard allowed the determination of the number of alkylsiloxanes on the substrate.
8. W. Gao and L. Reven, *Langmuir* **11**, 1860 (1995).
9. C. P. Tripp and M. L. Hair, *ibid.* **8**, 1120 (1992).
10. M. D. Porter, T. B. Bright, D. L. Allara, A. E. D. Chidsey, *J. Am. Chem. Soc.* **109**, 3559 (1987); C. D. Troughton *et al.*, *ibid.* **111**, 321 (1989); L. Netzer, R. Iscovici, J. Sagiv, *Thin Solid Films* **100**, 67 (1983).
11. L.-Q. Wang, J. Liu, G. J. Exarhos, B. C. Bunker, *Langmuir* **12**, 2663 (1996); A. Badia *et al.*, *ibid.*, p. 1262.
12. The 75.0-MHz ¹³C solid-state NMR experiments were carried out with a Chemagnetics spectrometer (300 MHz, 89-mm wide-bore Oxford magnet) using a double-resonance probe. For both pure and mercury-loaded FMMS samples, SP Bloch-decay and CP methods were used with ¹H decoupling. The dried powders were loaded into 7-mm zirconia rotors and spun at 3 to 4 kHz. Spectra were collected by an SP-excitation Bloch-decay method with a 5-μs (90°) ¹³C pulse and a 10-s repetition delay. For all experiments, 40-ms acquisition times and a 50-kHz spectral window were used. The number of transients was 1000 to 3000. The power levels of the carbon and proton channels were set so that the Hartmann-Hahn match was achieved at 55 kHz in CP experiments with contact times of 3 ms and repetition delays of 5 s. A Lorentzian line broadening of 24 Hz was used for all ¹³C spectra. The 59.3-MHz ²⁹Si NMR spectra were also taken for both samples using the SP Bloch-decay method with ¹H decoupling. A Lorentzian line broadening of 50 Hz and a repetition delay of 30 s were used for ²⁹Si spectra. Both ¹³C and ²⁹Si NMR chemical shifts were referenced to TMS at 0 ppm.
13. D. W. Sindorf and G. E. Maciel, *J. Am. Chem. Soc.* **105**, 3769 (1983).
14. EXAFS experiments on the mercury-laden FMMS were performed at the mMercury Lᵢᵢᵢ absorption edge on beamline X18B at the National Synchrotron Light Source. Measurements of tape mounts of mercury sulfide and mercury oxide standards were made in the transmission mode. Measurements on the FMMS samples were performed in the fluorescence mode, using the Stern-Heald configuration while simultaneously monitoring the absorption signal of the mercury sulfide reference on the downside of the experiment to allow investigation of the valence state of mercury in the sample. Data reduction and analysis were performed according to recommended procedures [E. A. Stern and S. M. Heald, *Rev. Sci. Instrum.* **50**, 1579 (1979); D. E. Sayers and B. A. Bunker, in *X-ray Absorption, Principles, Applications, Techniques of EXAFS, SEXAFS, and XANES*, D. C. Koningsberger and R. Prins, Eds. (Wiley, New York, 1988), pp. 211–256 and chap. 6]. The National Synchrotron Light Source at Brookhaven National Laboratory is supported by the U.S. Department of Energy, Office of Energy Research, Division of Materials Sciences and Division of Chemical Sciences.
15. U.S. Department of Energy, Mixed Waste Focus Area, *Technical Baseline Results* (World Wide Web: http://wastenot.inel.gov/mwfa/results.html); U.S. Department of Energy, *FY91 Waste and Hazard Minimization Accomplishments* (DOE Report MHSMP-91-37, Pantex Plant, Amarillo, TX, 1991); J. E. Klein, *Westinghouse Savannah River Company Inter-Office Memorandum SRT-HTS-94-0235* (11 July 1994).

16. S. Mitra, *Mercury in the Ecosystem* (Trans Tech, Lancaster, PA, 1986).
17. The tests with simulated waste were performed in batch mode. The waste solutions were mixed with FMMS powders at volume ratios of 20 to 100 at room temperature with agitation for 2 hours. The remaining metal concentrations in solutions were analyzed by cold vapor atomic absorption for mercury and by inductively coupled plasma–atomic emission spectroscopy (ICP-AES) for other metals. For hydrolytic stability, mercury-loaded FMMS was added to deionized water in a Teflon vessel and heated at 70°C for 24 hours. The original mercury concentration in the FMMS was 505 mg per gram of FMMS. After the heating, only 0.4% mercury was released from the materials. This is within the uncertainty involved in experimental procedures in which the mercury-loaded FMMS was washed to remove physically attached mercury before the release test. The regeneration test was performed as follows: Mercury-loaded FMMS was mixed with a concentrated HCl (12.1 M) solution for 4 hours. The solid materials were then separated by filtration. Analysis of the Hg concentration in the filtrate indicated that the mercury was 100% removed. The regenerated FMMS was used to treat a mercury nitrate solution. A mercury loading of 210 mg per gram of FMMS was obtained, corresponding to ~50% of the original loading capacity. The same results were obtained for a third regeneration and reuse cycle. Although the total loading capacity was reduced in regeneration, it still outperforms alternative materials. Some loading capacity was lost as a result of the oxidation of the thiol group and can be recovered by treating the regenerated materials with a reducing agent. Some loading capacity loss may also be attributable to the interactions of FMMS with strong acid, but the densely populated organic monolayers improved the stability of the silica-based materials, so that the FMMS was not dissolved even in concentrated acid and remained effective after the acid treatment.
18. Y. Otanl, H. Eml, C. Kanaoka, H. Nishino, *Environ. Sci. Technol.* **22** (no. 6), 70 (1988); K. A. Larson and J. M. Wiencek, *Environ. Prog.* **13** (no. 4), 253 (1994); S. E. Ghazy, *Sep. Sci. Technol.* **30**, 933 (1995); J. A. Ritter and J. P. Bibler, *Water Sci. Technol.* **25** (no. 3), 165 (1992).
19. A. R. Bishop and R. G. Nuzzo, *Curr. Opin. Colloid Interface Sci.* **1**, 127 (1996).
20. G. M. Whitesides, *Sci. Am.* **273**, 146 (September 1995); G. E. Fryxell *et al.*, *Langmuir* **12**, 5064 (1996).
21. B. C. Bunker *et al.*, *Science* **264**, 48 (1994); P. Calvert, *Nature* **334**, 651 (1988); _____ and P. Rieke, *Chem. Mater.* **8**, 1715 (1996).
22. Pacific Northwest National Laboratory is operated for the U.S. Department of Energy by Battelle under contract DE-AC06-76RLO 1830. We thank S. McGuire and W. Cosby for editorial assistance.

21 November 1996; accepted 4 March 1997

Manganese Oxide Mesoporous Structures: Mixed-Valent Semiconducting Catalysts

Zheng-Rong Tian, Wei Tong, Jin-Yun Wang, Nian-Gao Duan, Venkatesan V. Krishnan, Steven L. Suib*

Hexagonal and cubic phases of manganese oxide mesoporous structures (MOMS) have been prepared by means of the oxidation of $Mn(OH)_2$. The hexagonal MOMS materials form a hexagonal array of pores with an open porous structure, thick walls (1.7 nanometers), and exceptional thermal stability (1000°C). The walls of the mesopores are composed of microcrystallites of dense phases of Mn_2O_3 and Mn_3O_4, with MnO_6 octahedra as the primary building blocks. The calcined hexagonal MOMS have an electrical conductivity of 8.13×10^{-6} per ohm·centimeter, an average manganese oxidation state of 3.55, and a band gap of 2.46 electron volts. Catalytic oxidations of cyclohexane and *n*-hexane in aqueous solutions in a batch reactor show conversions of ~10 and ~8 percent, respectively. Characterization and catalytic data suggest that MOMS systems show significant enhancement in thermal stability with respect to octahedral molecular sieve materials.

Since their discovery at Mobil Corporation in 1992, mesoporous aluminosilicate materials (designated M41S) (*1*) have attracted considerable attention. Significant advances resulting from research in this area include novel properties of these materials (*2*), new synthetic chemistry (*1–4*), unique structures (*5*), and synthesis of related materials (*5*).

Oxides of transition metals have some advantages over aluminosilicate materials for use in electromagnetics, photoelectronics, and catalysis because transition metal atoms can exist in various oxidation states. However, syntheses and structures of transition metal oxides can be much more complicated than oxides of main group metals because of the multitude of different coordination numbers and oxidation states. Mesoporous structures of transition metals doped into aluminosilicates [Cr (*6*)] or transition metal oxides such as Ti (*7*), V (*8*), W (*3, 5*), Zn (*9*), Nb (*10*), and Ta (*11*) have been reported. Most of these transition metal oxide mesoporous materials are insulators with transition metals in isolated oxidation states.

Z.-R. Tian, W. Tong, J.-Y. Wang, Department of Chemistry, University of Connecticut, Storrs, CT 06269–4060, USA.
N.-G. Duan, Institute of Materials Science, University of Connecticut, Storrs, CT 06269, USA.
V. V. Krishnan, Department of Chemical Engineering, University of Connecticut, Storrs, CT 06269, USA.
S. L. Suib, Departments of Chemistry and Chemical Engineering and Institute of Materials Science, University of Connecticut, Storrs, CT 06269, USA.

*To whom correspondence should be addressed.

The generation of mixed-valent transition metal oxide mesoporous materials might lead to versatile systems for redox catalysis and battery applications (*12*).

The wall materials of the mesoporous aluminosilicate and transition metal oxide materials discussed above are believed to be composed of noncrystalline amorphous phases (*1, 3, 13*), that is, the materials can be viewed as glasses with ordered pores. There is considerable interest in determining the coordination numbers of the metal atoms (primary structure) and local structure of the wall materials (secondary structure) because the amorphous (local structure) nature of the walls has been largely unexplored.

We report here the synthesis of semiconducting mixed-valent manganese oxide mesoporous structures (MOMS), which are believed to consist of crystalline wall material and are related to octahedral molecular sieve (OMS) materials (*12, 14, 15*). Mixed-valent MOMS systems may represent a distinct family of mesoporous materials.

Cetyltrimethylammonium bromide (CTAB) cationic surfactants were used as micellar templates in water. Air and inexpensive chemicals ($MnCl_2$ and NaOH) were used as starting materials (*16*). Precursors were prepared by two distinct steps: (i) the formation of a layered phase of $Mn(OH)_2$ and the generation of an aqueous solution of surfactant in a separate system (*16*) and (ii) the mixing of the two systems such that the crystallites of layered $Mn(OH)_2$ reacted with the surfactants, leading to the formation of a mesoporous phase (*16*). The crystalline layered phase of $Mn(OH)_2$ was then mildly oxidized in air to form a mixed-valent manganese oxide shell (*16*). Finally, surfactant templates were removed by further oxidation during calcination, leading to the formation of a semiconducting mesoporous material (*16*). The control of the primary building block units and oxidation processes are the basis for developing our syntheses.

If the mixing step is done in air, some Mn^{2+} present in $Mn(OH)_2$ can be readily oxidized to Mn^{3+} and Mn^{4+} (*12, 14, 15*). This type of oxidation process has been observed in many of the syntheses of manganese oxide OMS phases, where mixtures are white [$Mn(OH)_2$] under N_2 atmosphere but brown (MnO_2, Mn_2O_3, or Mn_3O_4) under oxidizing atmospheres. The cylindrical micelles then react with two different building blocks [$Mn(OH)_6$ and MnO_6]. The oxidative atmosphere used during synthesis also provides a pathway to mixed valency and the possibility of forming edge-shared MnO_6 octahedra.

The $Mn(OH)_2$ is a white, layered crystalline material built from the edge-sharing of [$Mn(OH)_6$]$^{4-}$ octahedral clusters (*17*).

Oxidation of $Mn(OH)_2$ can readily produce brown to dark-gray phases of manganese oxides (*17*). The negatively charged building blocks of [$Mn(OH)_6$]$^{4-}$ of the $Mn(OH)_2$ microcrystallites have a higher probability of binding to positively charged surfactant head groups than of binding to one another. This bias may limit the size of the $Mn(OH)_2$ crystallites. The $Mn(OH)_2$ crystallites oxidize in air in the presence of surfactant much more quickly than they do in the absence of surfactant because the smaller $Mn(OH)_2$ particles react with O_2 faster and more completely. Microcrystallites of $Mn(OH)_2$ react with surfactants to eventually form mesoporous phases by means of self-assembly, with the help of large, cylindrical micelle templates.

Our x-ray diffraction (XRD) patterns (*18*) of the resultant solids (Fig. 1) suggest that the primary building blocks are octahedral MnO_6 units that link together to produce crystalline wall material. Similar XRD patterns were observed for these materials after heating to 1000°C.

Calcined samples prepared with a CTAB concentration of 28 weight % have arrays of pores of hexagonal shape (Fig. 2). This hexagonal symmetry is believed to be due to the organization of micelles, not the geometry of the primary building blocks of manganese oxide. The high degree of ordering is in direct contrast to reports of M41S mesopore systems (*1, 3*) and OMS systems (*12, 14, 15*). Electron paramagnetic resonance (EPR) data (*18*) suggest that the primary building blocks of the wall materials are octahedral MnO_6 units.

Argon sorption data (*19*) (Fig. 3) from Brunauer, Emmett, and Teller (BET) measurements and pore-size distribution data show that mesopores exist in these materials, and XRD, transmission electron micros-
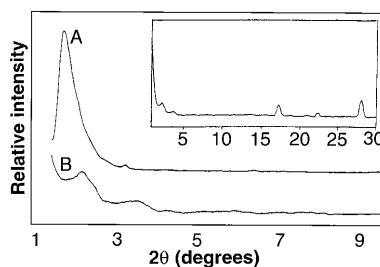
copy (TEM), and EPR data show that these are hexagonal MOMS materials, hereafter called MOMS-1. Cubic-phase XRD patterns were observed for materials prepared with a CTAB concentration of 10 weight %, with two peaks for the as-prepared material but seven peaks after calcination at 600°C (*18*). The surface area for this calcined cubic sample is 46 m^2 g^{-1}. This cubic phase will hereafter be referred to as MOMS-2.

The wall thickness of the mesopores, about 1.7 nm, was deduced from the interlattice *d* spacing of the (100) reflection (4.7 nm in Fig. 1A) and the pore diameter (3.0 nm) determined for the hexagonal MOMS-1 material. These data suggest that MOMS-1 consists of thick walls. The walls of MOMS-1 are also more dense than the walls of M41S materials, because Mn atoms are heavier than Si and Al atoms and the edge-shared MnO_6 octahedra are more tightly packed than the more flexible vertex-shared SiO_4 and AlO_4 tetrahedra. Subsequent oxidation of the manganese oxide wall materials is necessary for formation of edge-shared structures (*17*). Too much reduction to Mn^{2+} or to Mn^{3+} leads to reduced nonporous materials. Corner-shared tetrahedra are expected to be more flexible than edge-
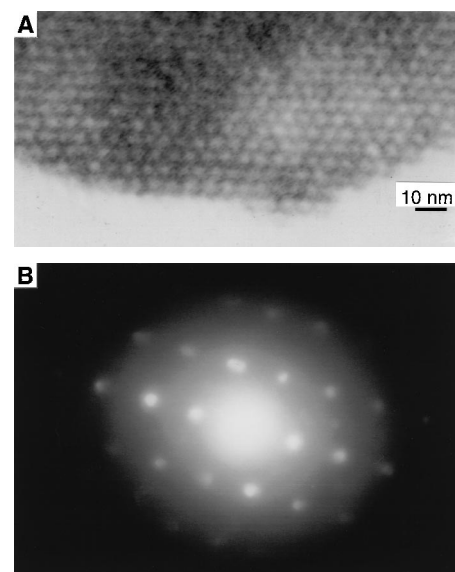
Fig. 2. (**A**) Lattice morphology of the calcined hexagonal MOMS-1 (CTAB concentration = 28%) shown by HRTEM. Crystallites with an average particle size of 200 Å are observed with no evidence of any other phase. (**B**) Convergent beam electron diffraction (CBED) pattern of the calcined hexagonal MOMS-1 showing hexagonal symmetry. The nonideal 120° angles for the MnO_6 octahedral building blocks suggest some stacking stress in these systems. Ordering of MOMS-1 in two dimensions shows nine orders of observed reflections. Stacking faults and twinning, observed in some OMS systems, were not observed in MOMS-1 or MOMS-2.

Fig. 1. (Curve A) XRD pattern of the uncalcined hexagonal MOMS-1. Note the strong (100) peak (*d* = 4.7 nm) and small (110) peak (*d* = 2.7 nm). (Curve B) XRD pattern of calcined hexagonal MOMS-1. The positions of the (100) and (110) peaks shifted to lower *d* spacings, and the peak intensities decreased. (Inset) The XRD patterns of calcined samples show two additional broad peaks (*d* = 0.50 and 0.30 nm), which are Mn_2O_3 (gamma phase) and Mn_3O_4 (hausmannite) microcrystallite phases.

shared octahedra. A large number of relatively rigid edge-shared MnO_6 octahedra may be needed to form a hexagonal MOMS-1 array. Similar thick, dense walls are proposed for the cubic MOMS-2 materials on the basis of corresponding XRD, high-resolution TEM (HRTEM), and adsorption data.

The shapes of the hysteresis loop in the adsorption-desorption isotherms of the calcined samples (Fig. 3B) are indicative of mesopores that are poorly defined (20) and may further support the thick and dense wall structure for MOMS-1. The Ar sorption data at low relative pressure ($P/P_0 \sim 10^{-5}$) (Fig. 3A) suggest that no micropores are present in these systems. The adsorption data further support data from XRD and HRTEM experiments that suggest that neither crystalline nor amorphous (15) microporous impurity phases are present in MOMS-1 or MOMS-2.

The average oxidation state (AOS) of MOMS-1 (Table 1) changes from a majority of 3^+ before oxidation to a majority of 4^+ after calcination. Changes in AOS are related to the ability of MnO_6 units to form mixed-valent microporous (12, 14, 15) and mesoporous systems by means of edge and vertex sharing.

The conductivities (22) of MOMS-1 before and after calcination are 5.0×10^{-8} and 8.1×10^{-6} (ohm·cm)$^{-1}$, respectively. Diffuse-reflectance ultraviolet-visible (DRUV-Vis) data (21) of the as-prepared MOMS-1 sample show an absorption at 390 nm, corresponding to a band gap (23) of 3.18 eV. The calcined MOMS-1 sample shows a DRUV-Vis peak at 505 nm, corresponding to a band gap of 2.46 eV. The conductivity
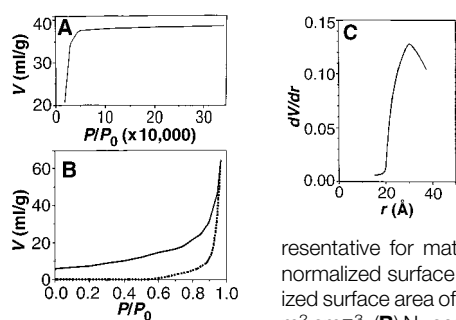
of the calcined MOMS-2 cubic phase is 2.28×10^{-6} (ohm·cm)$^{-1}$. Conductivities of the calcined MOMS-1 and MOMS-2 samples show temperature-dependent semiconducting behavior. Fermi level shifts (23) due to quantum size effects for Mn_2O_3 and Mn_3O_4 microcrystallites and the mesopore size of ~3.0 nm may have some effect on the conductivity. The conductivity of microporous todorokite-type OMS-1 crystalline phases (14) with similar AOS values of 3.5 (MOMS-1 = 3.55) is about 2×10^{-7} (ohm·cm)$^{-1}$ [MOMS-1 = 8.13×10^{-6} (ohm·cm)$^{-1}$], and pure dense-phase Mn_2O_3 has a conductivity of 5.0×10^{-8} (ohm·cm)$^{-1}$. Calcined MOMS-1 thus has a higher conductivity than synthetic todorokite, although both have similar AOS values, suggesting that special structural features of MOMS-1 may play an important role in the electrical conduction.

Oxidation with air converts the Mn^{2+} in the surfactant $Mn(OH)_2$ material into Mn^{3+} and Mn^{4+} as it does in microporous OMS materials. The $Mn(OH)_2$ layers closest to the micelle may not be reached by O_2 because of diffusion limitations of O_2 through unusually thick and dense walls in the initial mild oxidation step. In the following oxidation step, the structure may be stabilized by strong bonding of the negatively charged innermost $Mn(OH)_2$ layers to the positively charged surfaces of surfactant micelles. The structure may be further stabilized during calcination by the formation of hexagonal arrays of thermally stable outer MnO_2 layers. The color change from brown (Mn^{3+}) before calcination to almost black (Mn^{4+}) after calcination suggests that

the removal of surfactant during calcination was accompanied by further oxidation of wall material. Such color changes are in agreement with our proposal that the primary structural units are MnO_6 units and that crystalline dense-phase microcrystallites of manganese oxides in the walls are the secondary structural units of the MOMS systems. This two-step oxidation mechanism is supported by several observations, including changes in the color, AOS, conductivity, and band gap of the samples after calcination.

Calcined samples heated to 1000°C show a 4% weight loss, as shown in thermogravimetric analysis (TGA) data (19). This small weight loss may be due to the evolution of leftover surfactant or hydroxyl groups. Differential scanning calorimetry (DSC) data (19) do not show any clear phase changes for the heated calcined sample. The DSC and TGA data suggest that surfactant molecules are not present in the calcined samples because melting of the surfactant phase was not observed. These thermal data suggest that the calcined hexagonal MOMS-1 structure is thermally stable to 1000°C, which is also in agreement with XRD studies. The cubic MOMS-2 materials show similar TGA and DSC properties with thermally stable crystalline phases being observed up to 1000°C.

In microporous OMSs consisting of primary MnO_6 building blocks, the thermal stability decreases as pore size increases. The high thermal stability of these MOMS phases is unusual for manganese oxide systems. Fourier transform infrared (FTIR) data (19) for pyridine adsorbed on calcined MOMS-1 (Fig. 4) suggest that there are two types of acid sites that coexist on the surface of calcined MOMS-1: The surface is dominated by Lewis acid sites, which is usual for manganese oxide systems, as most crystalline microporous OMS materials have an overwhelming majority of Lewis acid sites. There is little

Fig. 3. (A) Low–relative pressure Ar sorption isotherm for the calcined hexagonal MOMS-1; V is the volume adsorbed per gram of MOMS-1. Saturation is reached at low relative pressure ($P/P_0 \sim 10^{-5}$). Relatively low surface areas (170 m^2 g^{-1}) are related to the dense, thick wall structure and are similar to microporous crystalline OMS phases (12, 14, 15) and mesoporous manganese nodules (27). Classical surface areas may not be truly representative for materials with transition metals like MOMS: A density-normalized surface area may be more appropriate. The density-normalized surface area of MOMS-1 is 886 m^2 cm^{-3} and that of MOMS-2 is 250 m^2 cm^{-3}. (B) N_2 sorption hysteresis for the calcined hexagonal MOMS-1. A clear hysteresis loop for adsorption-desorption is observed. (C) Pore size (radius r) distribution for the calcined hexagonal MOMS-1. The broad peak at about 30 Å is indicative of mesopores.
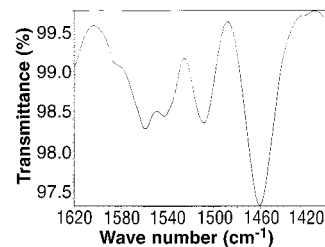

Fig. 4. FTIR spectrum for the pyridine on calcined hexagonal MOMS-1 showing an intense absorption at 1460 cm^{-1} and a considerably weaker absorption at 1540 cm^{-1}. The peak at 1460 cm^{-1} is due to Lewis acid sites and that at 1540 cm^{-1} is due to a much smaller number of Brönsted acid sites.

Table 1. Ratios of $Mn^{2+}:Mn^{3+}:Mn^{4+}$, average oxidation states, conductivities, and band gaps for uncalcined and calcined hexagonal MOMS-1.

MOMS-1	Ratio of $Mn^{2+}:Mn^{3+}:Mn^{4+}$	Average oxidation state (AOS)	Conductivity (ohm·cm)$^{-1}$	Band gap (eV)
Uncalcined	1:8.60:2.37	3.11	5.0×10^{-8}	3.18
Calcined	1:21.7:30.2	3.55	8.13×10^{-6}	2.46

information on the acidity of M41S materials (*24*).

However, temperature-programmed desorption (TPD) data for NH₃ adsorbed on calcined MCM-41 systems (*24*) and similar data for MOMS-1 show significant differences in the acidity of these two classes of materials. In the MCM-41 systems, the NH₃ TPD data mimicked behavior for amorphous silica aluminas with a relatively broad desorption. The NH₃ TPD data for MOMS-1 show three distinct peaks: at 215°C, between 300° and 310°C, and at 490°C. Such behavior is more typical for crystalline systems like zeolites and is in line with XRD data and the dense, thick structure of the crystalline walls of MOMS.

Data for the catalytic oxidation of cyclohexane (*25*) were obtained for calcined MOMS-1 (Table 2). The catalytic oxidation of stable alkanes to more valuable products like alkyl alcohols and ketones under mild reaction conditions is known to be catalyzed by mixed-valent microporous manganese oxide OMSs (*26*). Reactions of hydrogen peroxide with alkanes in the presence of manganese oxide OMS materials have been studied (*26*), and the role of lattice oxygen in catalytic oxidations has also been discussed (*14, 15*). These catalytic data suggest that MOMS-1 materials can function as active and selective oxidation catalysts and that total oxidation to CO₂ can be avoided.

Results of NH₃ TPD suggest that these reactions are driven by redox reactions, as previously suggested (*12, 14, 15, 26*) for microporous OMS systems. The catalytic data of Table 2 are also in line with suggestions of shape-selective redox catalysis at internal sites, because the smallest pore material, OMS-2, which has square pores (4.6 Å on a side, 6.5 Å in diameter), is most active and selective in these oxidations (*26*). The activities and selectivities of large-pore OMS-1 (6.9 Å on an edge, 9.7 Å

in diameter) are similar to those for the hexagonal MOMS-1 materials.

The total conversion and yields for *n*-hexane over MOMS-1 (Table 2) are promising, indicating that the total conversion of hexane and the less-stable cyclohexane are similar. The yields of both 2- and 3-hexanol are about one order of magnitude higher than the yield of 1-hexanol, probably because of thermodynamic constraints.

The catalytic oxidation of alkanes shown here suggests that the mesoporous hexagonal phase is active because of a redox mechanism that is a direct result of the mixed valency and unusually high thermal stability of MOMS materials. Future work should be aimed at understanding the interactions between surfactant molecules and Mn(OH)₂ materials, the nature of bonding in such systems, the effects of doping the wall phases, the local electronic environments, and other kinds of applications.

REFERENCES AND NOTES

1. C. T. Kresge, M. E. Leonowicz, W. J. Roth, J. C. Vartuli, J. S. Beck, *Nature* **359**, 710 (1992); J. S. Beck *et al.*, *J. Am. Chem. Soc.* **114**, 10834 (1992).
2. T. Maschmeyer, F. Rey, G. Sankar, J. M. Thomas, *Nature* **378**, 159 (1995).
3. Q. Huo, D. I. Margolese, G. D. Stucky, *Chem. Mater.* **8**, 1147 (1996); Q. Huo *et al.*, *Nature* **368**, 317 (1994), and references therein.
4. P. T. Tanev and T. J. Pinnavaia, *Science* **267**, 865 (1995); S. A. Bagshaw, E. Prouzet, T. J. Pinnavaia, *ibid.* **269**, 1242 (1995); G. S. Attard, J. C. Glyde, C. G. Gottner, *Nature* **378**, 366 (1995).
5. A. Firouzi *et al.*, *Science* **267**, 1138 (1995).
6. C. Otero Arean *et al.*, *Mater. Chem. Phys.* **34**, 214 (1993).
7. D. M. Antonelli and J. Y. Ying, *Angew. Chem. Int. Ed. Engl.* **34**, 2014 (1995).
8. T. Abe, A. Taguchi, M. Iwamoto, *Chem. Mater.* **7**, 1429 (1995); V. Luca, D. J. MacLachlan, J. M. Hook, R. Withers, *ibid.*, p. 2220.
9. D. Zhao and D. Goldfarb, *ibid.* **8**, 2571 (1996).
10. D. M. Antonelli and J. Y. Ying, *Angew. Chem. Int. Ed. Engl.* **35**, 426 (1996).
11. _____, *Chem. Mater.* **8**, 874 (1996).
12. Y. F. Shen *et al.*, *Science* **260**, 511 (1993).
13. A. Sayari, in *Recent Advances and New Horizons in Zeolite Science and Technology*, H. Chon, S. I. Woo, S. E. Park, Eds. (Studies in Surface Science and Catalysis 102, Elsevier Science, Amsterdam, 1996), pp. 1–46; B. P. Feuston and J. B. Higgins, *J. Phys. Chem.* **98**, 4459 (1994).
14. R. N. De Guzman *et al.*, *Chem. Mater.* **7**, 1286 (1995); Y. F. Shen, S. L. Suib, C. L. O'Young, *J. Am. Chem. Soc.* **116**, 11020 (1994).
15. H. Cao and S. L. Suib, *J. Am. Chem. Soc.* **116**, 5334 (1994); J. C. Lin, J. Chen, S. L. Suib, M. Cutlip, J. Freihaut, *J. Catal.* **161**, 659 (1996). Data from TEM and XRD show no evidence of other phases or amorphous species. Extensive studies of amorphous manganese oxides show that amorphous systems readily lose oxygen from room temperature to less than 100°C, eventually leading to particle growth of crystalline reduced phases of manganese oxides, which is not observed here. MOMS do not desorb oxygen at low temperature and show no generation of reduced phases up to 1000°C. Thermal, conductivity, analytical, EPR, and density data also argue against the presence of large amounts of amorphous material in MOMS.
16. We prepared MOMS-1 by dissolving MnCl₂·4H₂O [1.18 g in 15 ml of distilled deionized water (DDW)], which reacts with NaOH to produce Mn(OH)₂. A

28% aqueous surfactant solution of CTAB (6.67 g in 15 ml of DDW) was mixed with the Mn(OH)₂ and stirred at 75°C, further stirred for 30 min, and then heated for 12 hours at 75°C. The supernatant was then decanted, and the solid residue was washed six times with DDW, dried in air at ambient temperature, and calcined in air at 550°C for 3 hours. We prepared MOMS-2 from a 10% CTAB solution calcined in air at 400° and 600°C for 2 hours. The Mn(OH)₂ precipitates at pH = 8.0 and when dried in air is brown. After calcination, the color changed to black. After addition of CTAB aqueous solution of pH 7.0, the pH of the mixture was 6.0.
17. A. F. Wells, *Structural Inorganic Chemistry* (Clarendon, Oxford, ed. 4, 1975), pp. 209–214 and 519–521.
18. The XRD data were collected on a Scintag XDS-2000 θ-θ diffractometer (Cu Kα radiation, 45 kV, and 40 mA). All seven peaks of MOMS-2 can be indexed to a cubic system. Reorganization of edge- and vertex-shared MnO₆ groups due to changes in mixed valency during calcination of MOMS-2 may lead to the observed enhanced ordering. The XRD baselines were flat, and there were no sharp peaks in the XRD patterns of MOMS-1 or MOMS-2 from impure dense-phase crystalline manganese oxides. The HRTEM data [Philips CM 200 FEG (Super Twin-α Objective lens) operated at 200 kV; images were taken at a magnification of 580,000 and enlarged 2.87 times] were collected on calcined samples dispersed in acetone, which were supported on a holy carbon grid. A Bruker Electron Spin Resonance ESP 300 spectrometer was used to obtain EPR spectra, which show a hyperfine splitting of six lines centered at 3300 G that are separated by 92.8 G for calcined samples at 4.2 K, indicative of octahedral symmetry.
19. A DuPont DSC and a DuPont 951 TGA instrument were used under N₂ atmosphere with heating rates of 10°C min⁻¹. Omnisorp 100 CX and Cahn 2000 Microbalance instruments were used to determine surface areas and pore-size distributions. A static sorption vacuum system with a homemade quartz in situ cell with KBr windows was used for pyridine adsorption experiments on calcined samples. A Nicolet 750 FTIR spectrometer was used for diffuse-reflectance FTIR experiments.
20. U. Ciesla, S. Schacht, G. D. Stucky, K. K. Unger, F. Schuth, *Angew. Chem. Int. Ed. Engl.* **35**, 541 (1996).
21. Electropotential titrations [D. Glover, B. Schumm Jr., A. Kozowa, *Handbook of Manganese Dioxides Battery Grade* (International Battery Materials Association, Needham, MA, 1989)] were used to obtain AOS. Ratios of Mn²⁺:Mn³⁺:Mn⁴⁺ were determined with an Accumet pH Meter 25 from Fisher Scientific. We used (NH₄)₂SO₄ to leach the Mn²⁺ and HNO₃ to disproportionate Mn³⁺ into Mn²⁺ and Mn⁴⁺. We used KMnO₄ as the oxidizing titrant, and the potentiometric titration end point was 440 mV.
22. A Fell four-probe head combined with a Keithley 224 Programmable Current Source and a voltmeter were used to measure the conductivities of pressed sample pellets [L. Van der Pauw, *J. Phillips Res. Rep.* **13**, 1 (1958)]. The band gaps were calculated from powder UV-Vis spectra [A. R. West, *Solid State Chemistry and Its Applications* (Wiley, New York, 1984), pp. 75–78] collected on a Hewlett-Packard 8452A Diode Array Spectrophotometer equipped with a Labshere RSA-HP-84 Reflectance Spectroscopy Accessory.
23. A. R. West, *Solid State Chemistry and Its Applications* (Wiley, New York, 1984), pp. 82–85.
24. C. Y. Chen, H. X. Lin, M. E. Davis, *Microporous Mater.* **2**, 17 (1993); A. Liepold, K. Roos, W. Reschetilowski, *Chem. Eng. Sci.* **51**, 3007 (1996); A. Corma, V. Fornes, M. T. Navarro, J. Perez-Pariente, *J. Catal.* **148**, 569 (1994).
25. The reactions were carried out under reflux for 40 hours in aqueous solutions with stirring at 75°C. The reaction mixture contained 1.8 g of cyclohexane or *n*-hexane, 2.0 g of *tert*-butyl hydrogen peroxide (70% aqueous solution), 2.5 g of *tert*-butyl alcohol, 70 mg of calcined mesoporous material, and 0.1 g of acetophenone. The acetophenone (1.0 g, internal standard) was mixed with 25.0 g of *tert*-butyl alcohol

Table 2. Yields for the oxidation of cyclohexane and hexane over calcined hexagonal MOMS-1. The conversions for cyclohexane and *n*-hexane were 10.2 and 7.65%, respectively. No products were observed under similar reaction conditions when MOMS-1 catalyst was absent. Dashes indicate that the product was not observed.

Product	Yield (%)	
	Cyclohexane feed	*n*-Hexane feed
Cyclohexanol	2.6	–
Cyclohexanone	5.5	–
1-Hexanol	–	0.16
2-Hexanol	–	1.64
3-Hexanol	–	1.19
2- and 3-Hexanol	–	3.01

before it was added to the reactants. The reaction mixtures were analyzed by gas chromatography (GC) [HP-5890 GC equipped with a Supelcowax 10 fused silica column].
26. S. L. Suib, in *Recent Advances and New Horizons in Zeolite Science and Technology*, H. Chon, S. I. Woo, S. E. Park, Eds. (Studies in Surface Science and Catalysis 102, Elsevier Science, Amsterdam, 1996), pp. 47–74.
27. K. M. Parida, P. K. Satapathy, A. K. Sahoo, N. N. Das, *J. Colloid Interface Sci.* **173**, 112 (1995).
28. We acknowledge helpful discussions with M. E. Davis, A. Clearfield, C. T. Kresge, T. J. Pinnavaia, and G. D. Stucky. V. Chynwat is acknowledged for assistance with EPR experiments. We thank Y. Feng of Philips Electronic Instruments for help with HRTEM experiments. We acknowledge the U.S. Department of Energy, Office of Basic Energy Sciences, Division of Chemical Sciences, for support of this research.

Polarization-Enhanced NMR Spectroscopy of Biomolecules in Frozen Solution

Dennis A. Hall, Douglas C. Maus, Gary J. Gerfen, Souheil J. Inati, Lino R. Becerra,* Frederick W. Dahlquist, Robert G. Griffin†

Large dynamic nuclear polarization signal enhancements (up to a factor of 100) were obtained in the solid-state magic-angle spinning nuclear magnetic resonance (NMR) spectra of arginine and the protein T4 lysozyme in frozen glycerol-water solutions with the use of dynamic nuclear polarization. Polarization was transferred from the unpaired electrons of nitroxide free radicals to nuclear spins through microwave irradiation near the electron paramagnetic resonance frequency. This approach may be a generally applicable signal enhancement scheme for the high-resolution solid-state NMR spectroscopy of biomolecules.

$\mathbf{S}$ensitivity often dictates the feasibility of solid-state NMR (*1*) studies on chemical and biological systems. The small nuclear Zeeman energy splittings result in correspondingly small nuclear spin polarizations at thermal equilibrium. For example, protons exhibit a thermal equilibrium spin polarization of <0.01% at 5 T and 300 K.

We describe here a method that can substantially improve the sensitivity of high-resolution solid-state NMR spectroscopy of biomolecular systems in frozen glycerol-water solutions. We have obtained signal enhancements of up to $\sim$100 in the ^{13}C spectra of the amino acid arginine and $\sim$50 in the ^{15}N spectra of the 18.7-kD protein T4-lysozyme, which correspond to a large decrease in signal averaging time or sample size requirements, or both. Alternatively, this approach may permit the routine application of the expanding repertoire of multidimensional homo- and heteronuclear recoupling techniques (*2*) for performing spectral assignments and determining structural constraints in biomolecular systems such as large soluble proteins, nucleic acids, and membrane proteins.

D. A. Hall, D. C. Maus, G. J. Gerfen, L. R. Becerra, R. G. Griffin, Francis Bitter Magnet Laboratory and Department of Chemistry, Massachusetts Institute of Technology, Cambridge, MA 02139, USA.
S. J. Inati, Department of Physics, Massachusetts Institute of Technology, Cambridge, MA 02139, USA.
F. W. Dahlquist, Department of Chemistry, University of Oregon, Eugene, OR 97403, USA.

*Present address: Massachusetts General Hospital–NMR Center, Massachusetts General Hospital, Charlestown, MA 02129, USA.
†To whom correspondence should be addressed. E-mail: griffin@ccnmr.mit.edu

Dynamic nuclear polarization (DNP) (*3*) is used to transfer the high spin polarization of unpaired electrons to coupled nuclear spins through microwave irradiation at or near the electron paramagnetic resonance (EPR) frequency. Under optimal conditions, NMR signal intensities can be increased by the ratio of the electronic and nuclear Larmor frequencies, corresponding to factors of $\sim$660 and $\sim$2600 for ^1H and ^{13}C spins, respectively.

A number of signal enhancement schemes have recently been utilized in NMR spectroscopy, including optical pumping of quantum wells (*4*), photochemically induced DNP of photosynthetic reaction centers (*5*), polarization transfer from optically polarized xenon (*4, 6*) to surface and solution spins, and DNP of diamond, coal, and polymer systems doped with aromatic free radicals (*7–9*). These approaches have all proven successful for polarizing specific systems, but no method has yet been demonstrated to be generally applicable to macromolecular biological systems. Our DNP enhancement scheme uses a frozen aqueous (60:40 glycerol-water) solution doped with the nitroxide free radical 4-amino-TEMPO (2,2,6,6-tetramethyl-1-piperidinyloxy). Glycerol:water is frequently used as a cryoprotectant for protein samples in x-ray crystallography (*10*), and TEMPO and its analogs are commonly exploited for EPR spin-labeling studies on biological samples (*11*). Optimum DNP enhancement is achieved at $\sim$40 mM radical concentration (*12*).

In the DNP–cross-polarization (CP) pulse sequence (Fig. 1), polarization is first transferred from the 4-amino-TEMPO free radical to ^1H spins under microwave irradiation. Irradiation on the order of the nuclear spin-lattice relaxation time (T_1) is required for maximal polarization buildup. Proton spin diffusion distributes the enhanced magnetization throughout the solvent and solute during the irradiation period. Finally, a standard CP pulse sequence (*13*) transfers the high ^1H polarization to rare spins (typically ^{13}C or ^{15}N) for observation. The magnetic field is chosen to maximize the experimentally determined electron-to-proton polarization transfer efficiency (*14*).

Several mechanisms of electron-proton polarization transfer exist. In these experiments using 40 mM 4-amino-TEMPO in water-glycerol, DNP primarily proceeds through a thermal mixing mechanism (*8, 15*), in which irradiation off the center of the EPR line coupled with electron-electron cross-relaxation perturbs the electronic dipolar reservoir from thermal equilibrium. The nuclear spins become polarized through their coupling to the electronic dipolar reservoir. This coupling is induced by simultaneous spin flips of two electron spins differing in resonance frequency by the nuclear Zeeman splitting driving a nuclear spin flip (*16*). Thermal mixing involves irradiation of an allowed EPR transition, in contrast to another DNP mechanism, the solid effect, in which weak, second-order electron-nuclear spin flips are driven (*8*). Thermal mixing therefore requires less microwave power to achieve maximal enhancement, particularly in high magnetic fields where the probability of the solid effect transition is severely attenuated.
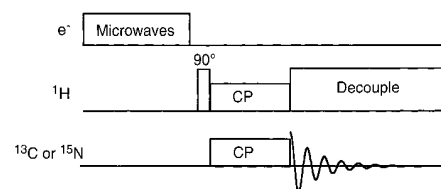

Fig. 1. Diagram of the DNP-CP pulse sequence. Initially, electronic polarization is transferred to proton spins by microwave irradiation for a period on the order of the ^1H T_1. The magnetic field is set to maximize the efficiency of polarization transfer. The proton polarization is then transferred to the rare nuclear spins (^{13}C or ^{15}N) by a standard cross-polarization sequence. Finally, the ^{13}C or ^{15}N spectrum is acquired while continuous-wave ^1H decoupling is performed.